

Research paper

Quantitative integration of sedimentological core descriptions and petrophysical data using high-resolution XRF core scans

S. Henares^{a,*}, M.E. Donselaar^{a,b}, M.R. Bloemsma^{c,d}, R. Tjallingii^e, B. De Wijn^{f,1}, G.J. Weltje^a^a Department of Earth and Environmental Sciences, Division of Geology, KU Leuven, Celestijnenlaan 200E, B-3001, Leuven, Belgium^b Department of Geoscience and Engineering, Delft University of Technology, Stevinweg 1, NL-2628CN, Delft, the Netherlands^c Advanced Sediment and Core Analysis Research (ASCAR), Minister van Houtenlaan 5, NL-1981EA, Velsen-Zuid, the Netherlands^d Tata Steel Europe, Centre of Expertise Iron Making, PO Box 10000, NL-1970CA, IJmuiden, the Netherlands^e GFZ German Research Centre for Geosciences, Section 'Climate Dynamics and Landscape Evolution', Telegrafenberg, GE-14473, Potsdam, Germany^f Wintershall Noordzee B.V., Bogaardplein 47, NL-2284, DP Rijswijk, the Netherlands

ARTICLE INFO

Keywords:

Data integration
XRF core scanning
Reservoir quality
Property prediction
Geochemical proxy data

ABSTRACT

In light of the huge investments needed to acquire sediment cores and the growing need of energy-providing companies to predict reservoir quality, it is remarkable that the standard workflow in core analysis has not been optimized to extract as much information from cores as possible. The Integrated Core Analysis (ICA) protocol presented in this study provides a statistical framework for multivariate calibration and prediction of a wide range of properties measured in core, based on integration of high-resolution X-ray fluorescence core-scanning (XRF-CS) proxy records with records of sparsely sampled petrophysical data and sedimentological core descriptions. The downscaling of numerical data involves the application of invertible transformations to remove range constraints on data, followed by calibration with Partial Least Squares regression through cross validation. Categorical data (i.e. lithofacies) are downsampled by associating each class with a statistical model based on the XRF-CS data. All data points are reassigned to their most likely class by applying Quadratic Discriminant Analysis. The result of the ICA is a multivariate data set in which all properties are specified at the same high resolution along the core with their prediction uncertainties. Downscaling of all variables to 1-cm vertical resolution permits investigation of the variability among petrophysical properties, geochemical proxies, and lithofacies memberships. Petrographic analysis is fundamental for interpretation of the XRF-CS records (element-mineral affinity) and for understanding the sedimentological controls on predicted petrophysical properties. Application of the ICA protocol to a 32 m thick, heterogeneous, Upper Carboniferous fluvial sandstone interval resulted in a near 30-fold increase of the petrophysical data base, which allowed identification of the main depositional and diagenetic controls on the spatial distribution of reservoir quality. Successful implementation of the novel ICA protocol will greatly increase the economic value of legacy core data in studies that aim to re-use depleted hydrocarbon reservoirs.

1. Introduction

Analysis of sediment cores is the only way to obtain direct measurements of salient properties of reservoir rocks in the subsurface, such as their porosity, permeability, chemical and mineralogical composition. Unique sources of geological information provided by cores are depositional setting, reservoir architecture, sediment provenance, and diagenetic history of reservoir rocks. The established workflow for routine core analysis (RCA) comprises petrophysical measurement of porosity, permeability, and grain density on core plugs (McPhee et al.,

2015) as well as a continuous sedimentological description of the core augmented by photographs, and it commonly involves petrographic analysis of a limited number of thin sections.

In light of the huge investments needed to acquire cores and the growing need of energy-providing companies to predict reservoir quality for a variety of subsurface applications, it is remarkable that the standard workflow in geological core analysis (Tavakoli, 2018) has not been optimized to extract as much information from cores as possible. The set of plug measurements only provides "spot" data of petrophysical properties, whose regular spacing (typically 25 cm) may vastly

^{*} Corresponding author.E-mail address: saturnina.henares@kuleuven.be (S. Henares).¹ Present address: Independent Geological Consultant, Palissander 151, Dordrecht, NL-3315MP, the Netherlands.

exceed the scale of vertical heterogeneity (bedding) of sediments. Even though the sedimentological log represents a continuous description according to an established lithofacies scheme (e.g. Reijers et al., 1993), it is not entirely clear at which resolution properties have been “averaged” by the sedimentologist to describe the core in terms of internally consistent sedimentary units (“mappable” lithofacies intervals). Hence, the lithofacies class assigned to each plug is the only firm connection between sedimentological and petrophysical data in the current RCA workflow.

The potential value of a sedimentological core description for prediction of petrophysical properties may be quantitatively assessed if a solid link can be established between sedimentological and petrophysical data by bringing them to the same resolution. On a conceptual level, this approach is based on the premise of Griffiths (1961), who stated that the fundamental properties of detrital sediments (grain-size, -shape, and -orientation, distributions, mineral composition, and packing) are all interrelated and contain sufficient information to predict derived properties such as petrophysical quantities. Following Griffiths (1961), it should be possible to rigorously integrate the separate RCA data to obtain one multivariate data set in which all properties are specified at the same high resolution along core (together with their uncertainties). Such a multivariate data set would be vastly superior to current RCA data, which comprise sets of measurements taken at different depths along a core, quite often with variable support (sampled volume) and/or spatial resolution (Baraka-Lokmane et al., 2009).

In the present paper, the term Integrated Core Analysis (ICA) is defined as a collection of procedures aimed at generating near-continuous multivariate time series of predicted rock properties with quantified uncertainties. The term near-continuous refers to the fact that in practice, measured properties are averaged over a certain volume or area. A logical choice for the characteristic spatial resolution of core data would be given by the diameter of core plugs from which RCA data are derived. The implementation of ICA presented in this study therefore provides predictions of all quantities of interest at a spatial resolution of 1 cm. The only way to tie together all possible data types is to connect them by means of measurements that may be acquired easily and non-destructively at the desired spatial resolution. Such measurements should contain sufficient information for establishing statistical links with the properties to be predicted.

In this paper, the implementation of the ICA protocol (Bloemsma, 2015; Weltje et al., 2017; Henares et al., 2018), makes use of X-ray fluorescence core scanning (XRF-CS) data as a multivariate proxy record from which a range of sediment properties may be predicted. It should be noted that in principle, there is no limit to the types of core data which may be predicted (e.g., the bulk chemical, mineral, and petrographic compositions, and the grain-size distribution), as long as the multivariate proxy record contains enough information about these properties. Instead of using XRF-CS data – as in this study – similar results may be achieved with near-infrared (NIR) spectroscopy (Hahn et al., 2018), or even better results by using both.

The purpose of this study is to present ICA as a generic statistical framework for robust core-data integration. Therefore, the statistical requirements for robust integration of numerical and categorical data (including prediction uncertainties) will be discussed first, and next, the generation of integrated core-data sets is shown. In the example presented, petrophysical spot measurements and continuous sedimentological core descriptions are embedded in a big-data environment provided by non-destructive XRF-CS records acquired at 1-cm vertical resolution. The added value of the ICA protocol for disentangling the geological controls on petrophysical properties is demonstrated by multivariate statistical analysis of an integrated core-data set of a fluvial sandstone reservoir (Upper Carboniferous, southern North Sea). Taking the RCA data set as a starting point, this study shows how the increased spatial resolution obtained after data integration allows refinement of the lithofacies distribution within the reservoir interval. In addition, each lithofacies may be fingerprinted by means of its distinct

detrital, diagenetic and petrophysical signatures, and its internal heterogeneity at cm-scale may be assessed. Successful implementation of the novel ICA protocol will greatly increase the economic value of legacy core data in studies that aim to re-use depleted hydrocarbon reservoirs in, for example, geothermal energy projects and CO₂ storage.

2. Methodology

2.1. High-resolution XRF-CS records

The proposed data-integration strategy relies on quantitative coupling of various data sets to a high-resolution proxy record of sediment properties and then use this relation to predict “missing” property values at every position along the core where a measurement is available. Suitable high-resolution records can be acquired with non-destructive X-ray fluorescence core scanners (XRF-CS) which have been used to measure element intensities directly at the core surface (Jansen et al., 1998; Croudace et al., 2006; Richter et al., 2006; Tjallingii et al., 2007; Bloemsma et al., 2018).

Because cores tend to be heterogeneous in terms of grain size, porosity, and contents of organic matter and water, the one-to-one relation between intensities and concentrations underlying conventional spectrum evaluation under standardized conditions does not generally hold for sets of related XRF-CS spectra measured in situ. Therefore, XRF-CS data have been regarded as semi-quantitative only and are primarily used for chemostratigraphic inter-well correlations.

A model for quantification of XRF-CS data under variable and unknown measurement conditions was proposed by Weltje and Tjallingii (2008), who combined theories of XRF spectroscopy and compositional data analysis to derive a calibration equation which is applicable to any pair of elements (denoted by subscripts *j* and *k*):

$$\ln\left(\frac{I_j}{I_k}\right) = \alpha_{jk} \ln\left(\frac{C_j}{C_k}\right) + \beta_{jk}$$

According to this model, log-ratios of element intensities (*I*) are unique linear transforms of log-ratios of element concentrations (*C*), where the stretch (α) and the shift (β) factors for the pair of elements under consideration represent the relative matrix effect and detection efficiency, respectively. Expressed in this form, the intensities are shown to be excellent proxies of chemical composition. The predictive power of the above calibration model and its multivariate extension has been demonstrated in various studies (Weltje and Tjallingii, 2008; Bloemsma et al., 2012; Weltje et al., 2015; Bloemsma, 2015). It should be noted that calibration of XRF-CS data is not always needed or desirable. The above calibration equation implies that elimination of the stretch and shift factors by standardization of intensities and concentrations in the log-ratio space would make the two data sets almost indistinguishable (ideally, their correlation matrices would become identical). Hence, there is nothing to be gained by calibration of intensities to chemical composition for the purpose of predicting petrophysical properties. Element intensities were processed and visualized using the free Xelerate software package (Bloemsma, 2015; Bloemsma et al., 2018).

2.2. Data-integration algorithms

2.2.1. Numerical data

Calibration to and prediction of numerical variables was carried out by means of Partial Least Squares (PLS) regression (also known as Projection to Latent Structures regression), an advanced calibration and prediction algorithm based on an unconstrained multivariate linear model (Abdi, 2010). Technically, it relies on orthogonalisation of the cross-covariance matrix of two multivariate data sets by Singular Value Decomposition (De Jong, 1993). In our case, these are the proxy data (XRF intensities) and the properties to be predicted (e.g. porosity or

Table 1

Transformations applied according to the type of data with their analytical inverses.

Variable type	Range	Transformation	Inverse	Example
Positive	$0 < x$	$y = \ln(x)$	$x = \exp(y)$	Permeability Grain density
Univariate compositional	$0 < x < 1$	$y = \text{alr}(x) = \ln\left(\frac{x}{1-x}\right)$	$x = \text{alr}^{-1}(y) = \frac{\exp(y)}{1+\exp(y)}$	Porosity
Multivariate compositional	$0 < x_j < 1$ $\sum_{j=1}^k x_j = 1$ $k > 2$	$y = \text{clr}(x)$ $= \left[\ln\left(\frac{x_1}{g(x)}\right), \dots, \ln\left(\frac{x_j}{g(x)}\right), \dots, \ln\left(\frac{x_k}{g(x)}\right) \right]$ $g(x) = \left(\prod_{j=1}^k x_j \right)^{1/k}$	$x = \text{clr}^{-1}(y)$ $= \left[\frac{\exp(y_1)}{s(y)}, \dots, \frac{\exp(y_j)}{s(y)}, \dots, \frac{\exp(y_k)}{s(y)} \right]$ $s(y) = \sum_{j=1}^k \exp(y_j)$	Element intensities (XRF) Chemical, mineralogical, petrographic compositions Grain-size distribution

permeability). In order to maximize its performance, constrained numerical variables are transformed prior to modelling such that any real value of this transformed variable is physically tractable (e.g., strictly positive permeabilities, porosities ranging between 0 and 100%). The purpose of these transformations is to align the statistical properties of the data and their inter-relationships as closely as possible with the requirements of the PLS model. In terms of range constraints, the numerical core data integrated in this study fall into three groups. Intrinsically positive data such as permeability and grain density are subjected to logarithmic transformation, univariate compositional data such as porosity (and its implicit complement, the solid volume fraction) are subjected to an additive log-ratio (alr) transformation, and compositional data with more than two components (such as chemical, mineral, petrographic compositions, grain-size distributions, and element intensities) are subjected to a centred log-ratio (clr) transformation (Aitchison, 1986). Table 1 lists each data type with its corresponding forward and inverse transformation.

After all variables have been appropriately transformed, their errors are assumed to be additive and approximately normally distributed. The unconstrained calibration problem is solved by using PLS regression with cross validation, so as to prevent overfitting of the calibration model (inclusion of noise), and derive an estimate of the uncertainty. Cross validation involves leaving out one observation from the calibration data, and predicting its value from a calibration model based on the remaining data points. The squared Euclidian distance between the measured and predicted quantities is defined as the squared cross-validation (or prediction) error, a direct measure of the model's predictive capability. By repeating this process for all data points the mean squared prediction error (MSPE) may be derived, which is taken as the measure of uncertainty for the predicted quantity. Because all transformations are mathematically invertible (Table 1), predicted values can always be represented in terms of native units (e.g. % or mD). After inverse transformation, all predicted values automatically obey the range constraints associated with those native units, and are thus physically realistic (i.e., negative permeabilities, porosities and concentrations are precluded, and concentrations will sum to unity).

2.2.2. Categorical data

Categorical data such as lithofacies class may be quantified by associating them with the set of XRF-CS data measured at corresponding core positions. The characteristics of each lithofacies were captured by a multivariate normal distribution of intensities in the clr-space (Aitchison, 1986). Assigning class memberships to objects on the basis of numerical data may be carried out by Discriminant Function Analysis. In order to get the most out of the data, Quadratic Discriminant Function Analysis (QDFA) is employed which uses stratified mean and covariance estimation, i.e., the mean XRF-CS signature and associated covariance matrix is estimated separately for every class (Lachenbruch and Goldstein, 1979). QDFA is applied to the core description by transforming it to a vector containing the assigned lithofacies class at every scanned core position. The prior probability assigned to each lithofacies class is equal to the proportion of each class in the calibration

data (assuming that the sedimentologist is right “on average”). The mean vector and variance-covariance matrix of the lithofacies classes permit each intensity measurement to be probabilistically assigned to one of the lithofacies classes by means of a quadratic discriminant function. The predicted class is then used to “downscale” the sedimentological core description to the resolution of the XRF-CS record.

3. Data sets

Continuous geochemical records were obtained at 1 cm-scale resolution on the slabbed and polished core surfaces with an Avaatech XRF core scanner (Jansen et al., 1998) at the Royal Netherlands Institute of Sea Research (NIOZ, Texel, NL, Bloemsma, 2015). Measurements were carried out at 10 kV and 30 kV with count time of 20 s and 15 s, respectively, and a tube current set at 1800 μA in both runs. Replicate measurements were taken every 25th core position and used to calculate uncertainties. Spectrum interpretation of the XRF output provided intensities of major and minor elements (Al, Si, S, K, Ca, Ti, Mn, Fe, Ga, Rb, Sr, Zr, Br, Y, Cu, Zn, Cl and Cr) that depend on the element concentration but also on matrix effects, physical properties, sample geometry, and hardware settings of the scanner.

A full macroscopic lithofacies description was made of a cored interval from an Upper Carboniferous (early Westphalian B) reservoir in the Cleaver Bank High area of the Dutch offshore (Ziegler, 1990; Geluk et al., 2002; Kosters and Donselaar, 2003, Fig. 1). The selected interval (32 m of the 73-m-long core) comprises fluvial sandstones of early Westphalian age bounded above and below by coal-bearing floodbasin deposits (Fig. 2). This interval represents two stacked reservoir units, as inferred from their different paleocurrent directions on image logs: NE to SE for Reservoir Unit 1 and SW for Reservoir Unit 2 (Fig. 2; Boels, 2003). The difference in transport directions might indicate a provenance shift at the boundary between the two units. Sedimentological heterogeneity in the selected reservoir interval renders this example highly appropriate for illustrating the ICA workflow.

Qualitative petrographic inspection by optical microscopy was carried out on 20 selected sandstone thin sections (Fig. 2) to characterise the main detrital and diagenetic components of the cored reservoir intervals. Selection of the samples was based on the combination of petrophysical and sedimentological data to ensure that lithofacies and poro-perm variability were adequately captured. In addition, the distribution in the clr-space of element intensities was taken into account, because petrography is fundamental for constraining interpretations of the chemical record (Weltje et al., 2017; Henares et al., 2018). Samples were etched and stained with hydrofluoric acid and Na-cobaltinitrite for plagioclase and K-feldspar identification, and with alizarin red-S and potassium ferricyanide for discrimination among carbonate types.

Values of the helium porosity and Klinkenberg permeability measured on horizontal plugs from the studied core interval were taken from Bakker and Pruno (2004). For the purpose of this study, the focus is on Reservoir units 1 and 2, from which 105 plugs were analysed (Table 2; Fig. 3A–C).

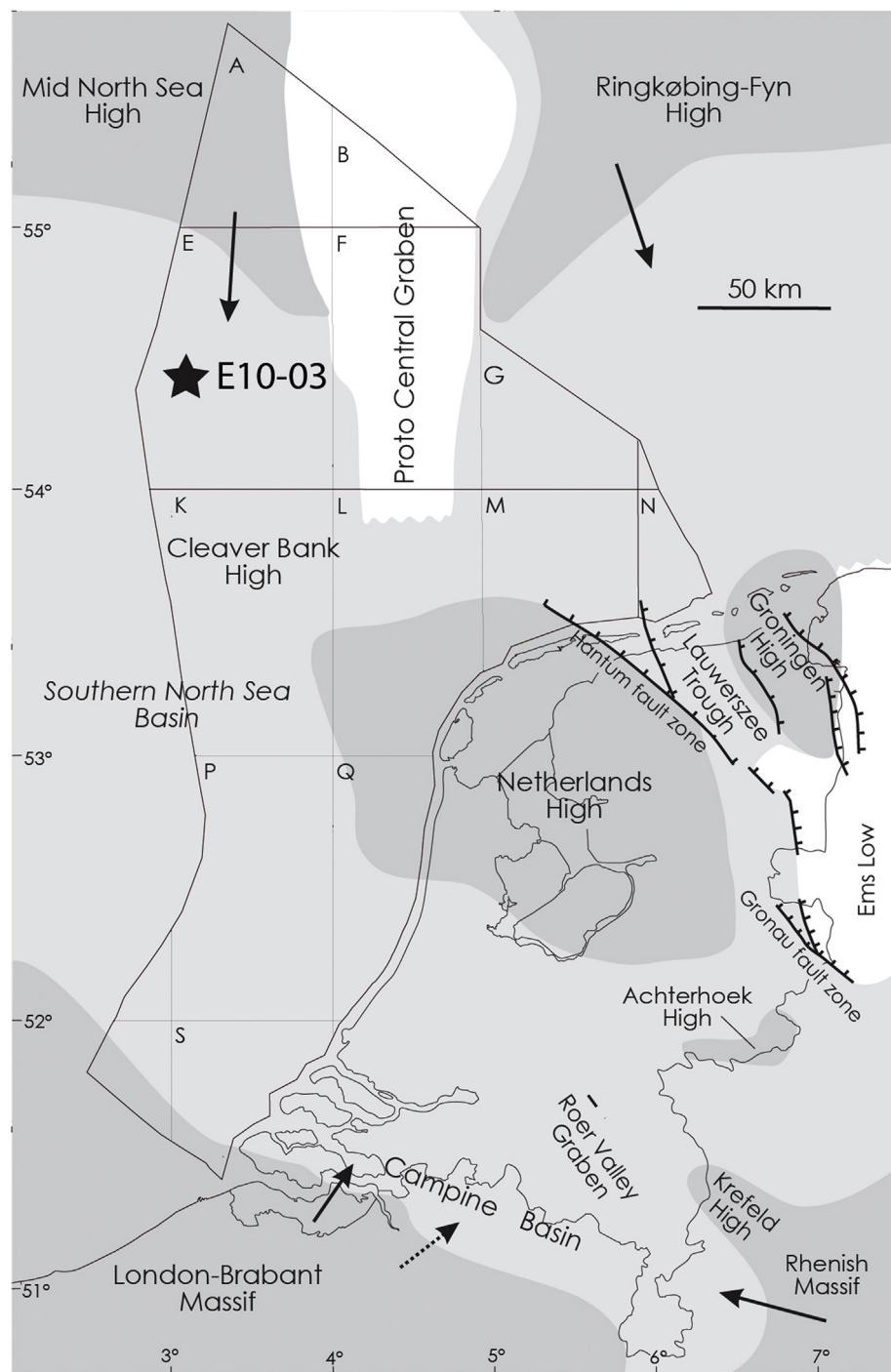


Fig. 1. Map of the Southern North Sea basin with main Westphalian structural elements and location of well E10-03. Arrows: main sediment transport paths (after Van Adrichem Boogaerd and Kouwe, 1993).

4. Results

4.1. Lithofacies associations and their petrophysical properties

The 32-m-thick studied interval is bounded below and above by mudstone, and comprises moderately to poorly-sorted, very fine-to very coarse-grained and gravelly, closely-stacked sandstone and associated fine-grained sandstone and mudstone (Fig. 2). There are two reservoir units (RU-1 and RU-2) with an overall net-to-gross of 0.96. Four lithofacies associations (LAs) are recognized on the basis of the sedimentary characteristics and petrophysical properties: fluvial sandstone (LA-1), gravelly fluvial sandstone (LA-2), fine-grained sandstone-

dominated overbank (or: proximal floodbasin) deposits (LA-3), and floodbasin mudstone (LA-4).

4.1.1. Lithofacies association 1 – fluvial sandstone

LA-1 occurs between 3693.5 and 3698.2 m in RU-1 and is characterized by medium-to coarse-grained, trough cross-bedded light-brown sandstone. The lower boundary of LA-1 (at 3698.20 m) is a sharp, erosional contact with the underlying floodbasin coal and claystone deposits (Fig. 2A). Medium grain size is dominant and the sandstone is moderately sorted with dispersed clay flakes, coal fragments (Fig. 2A) and small, oxidized rip-up clasts. Bed thicknesses are up to 1.4 m. Lower bed boundaries are sharp, erosional and flat, and lack

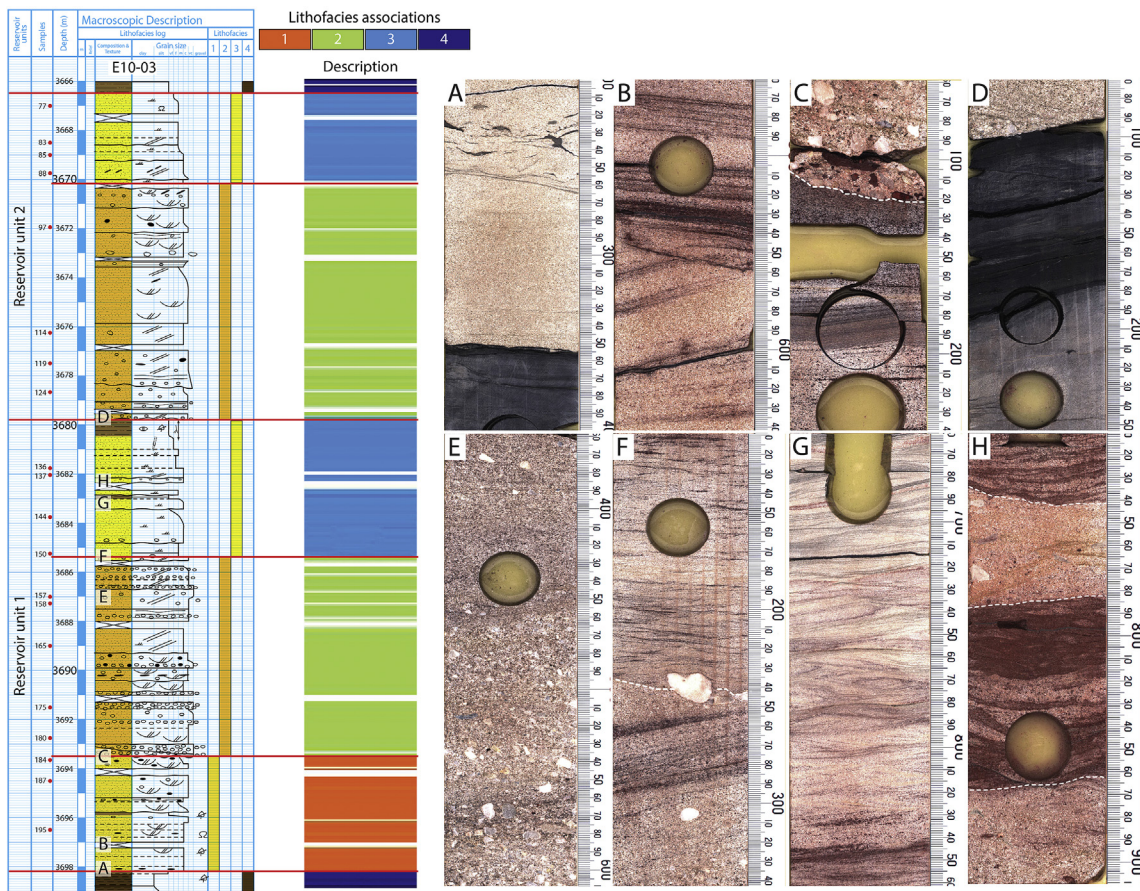


Fig. 2. Left log: Core description of the studied reservoir interval with lithofacies associations 1–4 and reservoir-unit subdivision. Numbered red dots: petrographic samples. Location of core photographs indicated from A to H. Middle log: Lithofacies description. Right pictures: Core photographs: A) Sharp, erosional contact between medium-grained sandstone (LA-1) and black, coal-bearing floodbasin claystone (3698.20 m). Note the dispersed coal fragment in the upper part. B) Moderately-sorted, medium-grained trough cross-bedded sandstone (LA-1). Cross-bedding accentuated with micaceous laminae (3697.10 m). C) Sharp, erosional contact between very coarse-grained sandstone with pebble lag (LA-2) and underlying moderately-sorted, medium-grained trough cross-bedded sandstone (LA-1) (3693.50 m). D) Sharp, erosional contact between coarse-grained sandstone with quartzite granules (LA-2) and underlying black, coal-bearing floodbasin siltstone (LA-3). E) LA-2. Poorly-sorted, coarse-to very coarse-grained sandstone with quartz granules and pebbles. Faint lamination (3687.00 m). F) Boundary between LA-2 and LA-3. Medium to fine-grained, well-sorted cross-laminated sandstone (LA-3) overlies poorly-sorted, cross-bedded coarse sandstone with quartz pebbles (LA-2). The cross-bed laminae are lined with Fe-oxide grains (3685.40 m). G) LA-3. Cm-scale medium to fine-grained, cross-laminated sandstone (3683.20 m). H) Interbedding of 4-cm-thick medium-grained sandstone with quartzite granules, and fine-grained, ripple-laminated sandstone (LA-3) (3682.30 m). (For interpretation of the references to colour in this figure legend, the reader is referred to the Web version of this article.)

coarse lag deposits. Cross-set heights vary from less than 10 cm–35 cm. The cross-bedding is accentuated by dark-brown, micaceous and Fe-oxidized laminae (Fig. 2B–C). The mean porosity and permeability values of LA-1 (12.2% and 0.8 mD, respectively) are intermediate when compared with the typical poro-perm values of LA-2 and LA-3 (Table 2; Fig. 3A).

4.1.2. Lithofacies association 2 – gravelly fluvial sandstone

LA-2 occurs in both reservoir units (RU-1: 3670.20–3679.75 m; RU-2: 3685.40–3693.50 m; Fig. 2). The contact of the lower LA-2 interval with the underlying LA-1 (at 3693.5 m) is sharp, erosional and undulating, and lined with large (up to 1.5 cm diameter) quartzite and oxidized claystone pebbles (Fig. 2C). Comparably, the contact of the upper LA-2 interval with the top of LA-3 at 3679.75 m is sharp, erosional and with a quartz pebble lag (Fig. 2D). Overall, LA-2 is characterized by grey to light-brown, very coarse-to medium-grained, poorly-sorted, massive to cross-bedded sandstone with quartz pebble stringers and dispersed granules (Fig. 2E–F). Lower bed boundaries are sharp, erosional and undulating and accentuated by lag deposits of quartzite and claystone granules and pebbles (Figs. 2C–2D–2F). Trough cross-bedding is the dominant sedimentary structure with deformed clay drapes and flakes lining the laminae. Cross-sets are up to 35 cm

thick. The LA-2 interval of RU-1 is coarser grained than that of RU-2, and shows a larger content of dispersed clay and quartzite granules and pebbles. Mean porosity and permeability of LA-2 show the highest values among the different LAs, i.e. 14.8% and 9 mD, respectively (Table 2; Fig. 3A–C). Differences between the mean poro-perm values of the two LA-2 intervals are minimal (Table 2; Fig. 3B and C).

4.1.3. Lithofacies association 3 – fine-grained overbank deposits

LA-3 occurs in both reservoir units (RU-1: 3666.45–3670.20 m; RU-2: 3679.75–3685.40 m). The contact between LA-3 and the underlying LA-2 (at 3685.4 m) is characterized by a sharp decrease in grain size and a change from cross-bedded (LA-2) to ripple-laminated sandstone (LA-3; Fig. 2F–G). The sandstone deposits are light-to red-brown and contain conspicuous red-brown, Fe-oxidized intervals (Fig. 2H). The sandstone is moderately sorted, and very-fine to medium grained. Multiple fining-upward grain-size successions occur in RU-1, and a single fining-upward grain-size succession in RU-2 (Fig. 2D). Thin layers (up to 5 cm-thick) with characteristics of LA-2 (i.e., medium-grained sandstone with dispersed quartz granules) are interbedded with the fine-grained ripple-laminated sandstone (e.g., at 3682.3 m; Fig. 2H). Flaser bedding and delicate ripple lamination, accentuated by micaceous laminae, are the most common sedimentary structures (Fig. 2F–G).

Table 2

Porosity and permeability distributions of raw data and their predicted values (in native units). LA = lithofacies association, RU = reservoir unit. Stats: M = mean in PLS space; S = sample standard deviation in PLS space; n = sample size.

Lithofacies/Reservoir Unit	Stats	Porosity (%)		Permeability (mD)	
		data	predict.	data	predict.
LA-1	M – S	9.6	9.9	0.10	0.14
	M	12.2	11.7	0.8	0.8
	M + S	15.3	13.9	6.4	4.7
	n	16	428	16	428
LA-2	M – S	11.5	11.5	0.8	0.6
	M	14.8	14.5	9.0	6.7
	M + S	18.8	18.3	106	83
	n	64	1655	64	1655
LA-2/RU-1	M – S	10.2	10.8	0.4	0.4
	M	14.3	14.4	9.1	7.3
	M + S	19.7	19.1	223	132
	n	30	800	30	800
LA-2/RU-2	M – S	10.2	12.2	0.4	0.8
	M	15.2	14.6	8.9	6.3
	M + S	17.6	17.4	45	50
	n	34	855	34	855
LA-3	M – S	7.6	6.5	0.012	0.005
	M	10.2	8.5	0.07	0.03
	M + S	13.6	11.2	0.42	0.15
	n	25	798	25	798
LA-3/RU-1	M – S	7.2	6.3	0.013	0.006
	M	9.9	8.3	0.08	0.04
	M + S	13.5	10.9	0.56	0.23
	n	14	427	14	427
LA-3/RU-2	M – S	8.0	6.7	0.012	0.003
	M	10.6	8.8	0.06	0.02
	M + S	13.9	11.5	0.30	0.09
	n	11	371	11	371

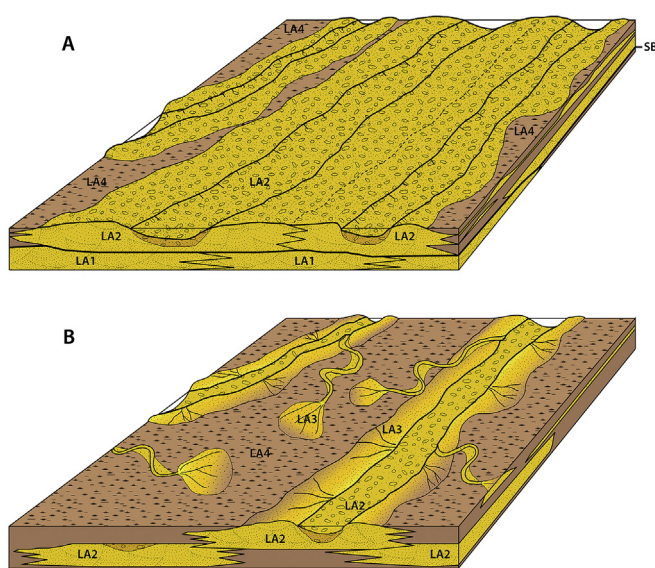


Fig. 4. A) Sequence boundary (SB) separates laterally-amalgamated coarse-grained low-sinuous fluvial deposits (LA-3) from underlying finer-grained fluvial sandstone. B) Relative base-level related flooding of the fluvial system. The inter-channel area is gradually filled with flood-basin fines (LA-4), terminal-splay and overbank sand (LA-3).

Mean porosity and permeability values are the lowest of the studied cored interval, 10.2% and 0.07 mD, respectively (Table 2; Fig. 3B and C). LA-3 in RU-1 shows the highest scatter of poro-perm values and is characterized by lower porosity but higher permeability than LA-3 in RU-2 (Table 2; Fig. 3B and C).

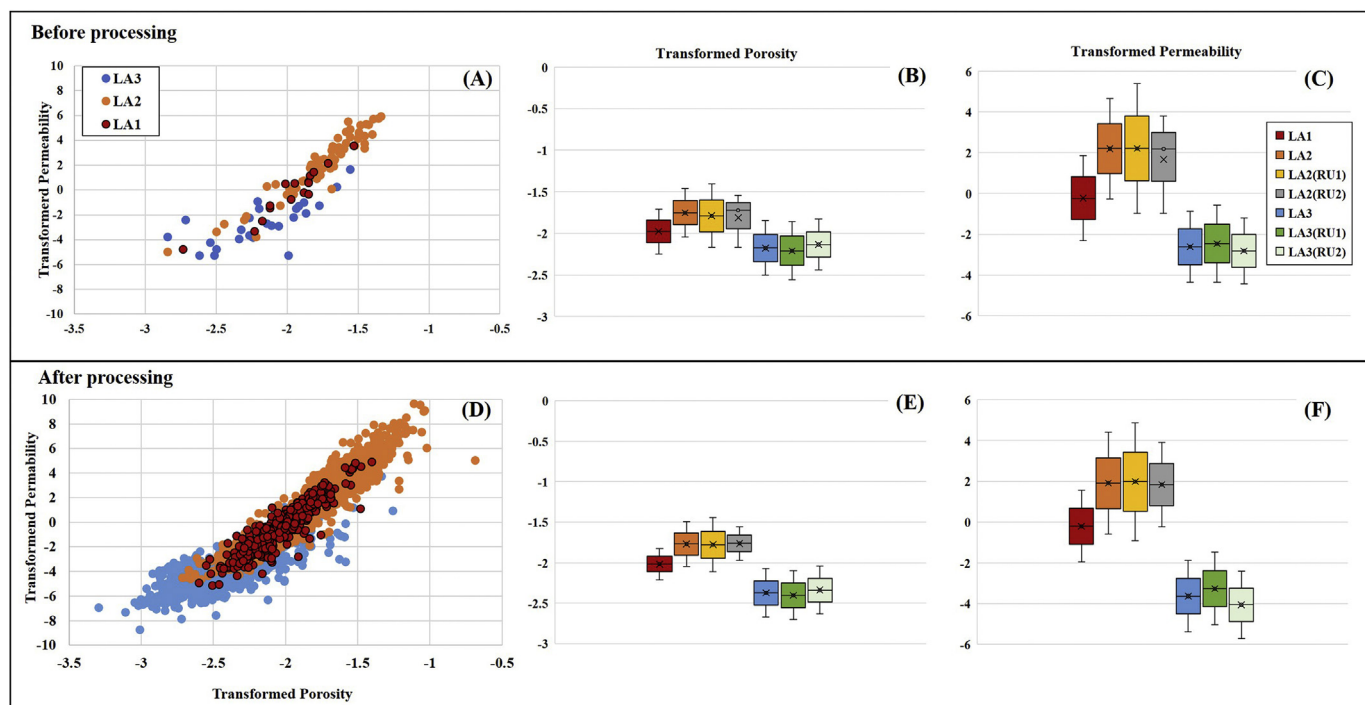


Fig. 3. A) Cross-plot of transformed poro-perm data colour-coded according to original LA. B) Boxplots showing the scatter of the aforementioned porosity and permeability values, respectively. D) Cross-plot of transformed poro-perm predictions colour-coded according to predicted LA. E) Boxplots showing the scatter of the aforementioned porosity and permeability values, respectively. Internal cross: arithmetic mean; internal horizontal line: median; upper and lower whiskers: maximum and minimum values, respectively. (For interpretation of the references to colour in this figure legend, the reader is referred to the Web version of this article.)

4.1.4. Lithofacies association 4 – floodbasin mudstone

LA-4 occurs below 3698.20 m (Fig. 2A) and above 3666.40 m. It consists of dark-grey to black, massive and laminated siltstone and subordinate claystone, and is rich in coal fragments and in-situ plant roots. The 5 to 10-cm-thick, sharp-based beds are fine grained, cross laminated and gradually fine upwards to siltstone. Petrophysical data of this LA were not taken into account.

4.1.5. Depositional setting

The fluvial deposits of LA-1 and LA-2 are the product of low-sinuous rivers (Fig. 4A). Individual sandstone beds lack fining-upward successions associated with meandering river deposits. Large-scale avalanche foresets, typical of braided-bar front accretion are lacking. The difference in lithofacies characteristics between LA-1 and LA-2 is the result of inter-annual peak discharge variability (Fielding et al., 2018). The dominant preserved cross-bedding (LA-1) points to low peak discharge variability, whereas the structureless intervals of LA-2 indicate reworking of the cross-sets in a regime with moderate peak-discharge variability. The multiple fining-upward successions in the lower LA-3 interval formed by sinuous rivers that entered the inter-channel floodbasin (Fig. 4B). The cm-scale ripple lamination in combination with preserved bedforms of LA-3 are typical of waning-flow overbank and terminal splay deposits (Van Toorenenburg et al., 2018) whereby sand settles out of suspension as the flow expands into the floodbasin and decelerates below the suspension threshold velocity.

The vertical successions of LA-1 to LA-2 (in RU-1) and LA-3 to LA-2 (transition RU-1 to RU-2) are interpreted as the result of base-level fall and associated basinward shift of fluvial facies, with the introduction of coarser lithofacies and extra-basinal components in LA-2. Sand-on-sand stacking (LA-2) with erosional contacts points to reduced rate of accommodation increase and implies lateral amalgamation of fluvial sandstones with low preservation potential of floodbasin fines (Fig. 4A). Superposition of LA-3 on LA-2 (upper part of RU-1 and RU-2) marks a base-level rise and increase of preservation potential of fine-grained floodbasin deposits (Fig. 4B). The change from LA-3 to LA-4 (top of the studied reservoir interval) is interpreted as continued base-level rise and flooding of the fluvial system.

4.2. Qualitative petrographic analysis

The detrital composition of the analysed sandstones is fairly uniform with non-undulatory monocrystalline quartz as the dominant grain type, followed by rock fragments represented by low-to medium-grade (phyllites and schists) metasedimentary and sedimentary (siltstone) grains, in order of decreasing abundance. Plutonic rock fragments are only observed in LA-2 of RU-2 (Fig. 5A). K-feldspars, when still present, are partially dissolved or replaced by kaolinite, illite and/or siderite (Fig. 5A, B and F). Other minor framework components are ultrastable heavy minerals (zircon-tourmaline-rutile) and micas, especially abundant in the finer-grained intervals of LA-3 (Fig. 5C and D), together with clay pebbles, mainly in LA-2, which are usually admixed with Fe-oxides and replaced by haematite or frambooidal pyrite (Fig. 5D).

Main porosity-modifying processes have been compaction (mechanical and chemical), cementation and dissolution. Mechanical compaction is favoured by the occurrence of ductile grains such as micas and clay clasts and flakes (Fig. 5C and E). Chemical compaction is more evident in LA-2 where it results in well-developed suture contacts between quartz grains (Fig. 5E). Main authigenic minerals include kaolinite, quartz overgrowths, Fe-dolomite and siderite. Vermiform kaolinite booklets are found as pore-filling and replacive types (Fig. 5F) in all the analysed lithofacies, and are particularly widespread in LA-2. Here, kaolinite, when coarse-grained, may show abundant micro-porosity. Euhedral quartz overgrowths also occur in the three described lithofacies but are particularly well-developed in LA-2 (Fig. 5G). Late carbonate cements, represented by Fe-dolomite and siderite, mainly occur in LA-1 and 3. Euhedral, poikilotopic, locally zoned Fe-dolomite

dominates over siderite and precipitates as pore-filling cement in both primary and secondary pores (Fig. 5H). Lozenge-shaped siderite often forms crystal clusters in secondary pores where K-feldspar relicts can be still recognized after partial dissolution (Fig. 5B).

4.3. Petrographically constrained geochemical analysis

Multivariate statistical analysis of the high-resolution XRF-CS data (Aitchison, 1986) is used to uncover meaningful geochemical associations in the light of the petrographic observations, and their relationship with the different lithofacies described (Fig. 6A and B). Principal components analysis (PCA) shows that 81% of the chemical variability within the studied core interval can be explained by the first three components (Fig. 6C). The covariance of the geochemical elements is conveniently visualized in biplots: vectors of two elements which are positively correlated will point in the same direction, and in opposite directions if they are negatively correlated. Two elements are uncorrelated if their vectors are approximately orthogonal. Accordingly, the following potential element-mineral affinities are identified in the clr-space:

Ca and Mn: the strong positive correlation between these elements suggest they are present in the same mineral phase, likely carbonate cements.

Ca and K: their strong negative correlation represents the replacement of detrital K-feldspars by carbonate cements.

Ca and Fe: their lack of correlation suggests a different mineralogical affinity for each one such as carbonate cements and haematite and/or pyrite, respectively.

Al, K, Rb, Ga and Sr: the marked positive correlation among these elements likely reflects the abundance of several framework components (e.g. K-feldspars, muscovite, clay clasts) and their associated diagenetic by-products (i.e. kaolinite, illite).

Ti and Zr: their positive correlation may be due to the presence of heavy minerals such as zircons, rutile, and titanite. Note also the marked positive correlation of these elements with the Al, K, Rb, Ga and Sr group which suggests a strong association between clay occurrence and heavy mineral concentration, likely due to hydraulic sorting.

On the biplot (Fig. 6A and B), the LA-1 data cluster is strongly related with elements such as Ca and Mn but also Si. There is a slight overlap between LA-3 and LA-1 data with respect to the presence of Ca. LA-2 shows a strong association with Si abundance and, to a minor extent, with Fe content. The partial overlap between LA-2 and LA-3 relates to the presence of Fe. Another subset of LA-3 data, which display the largest scatter, is associated with the Al, K, Rb, Ga, Sr, Ti and Zr group.

5. Data integration and interpretation

After the data integration, a continuous dataset has been generated which includes porosity and permeability values, lithofacies classification and element intensities at 1-cm resolution. In the present example, the size of the petrophysical data base has been increased almost 30-fold (from 105 to 2881 data points). The predicted petrophysical properties are shown in Fig. 7, side by side with the sedimentary log, the lithofacies description and prediction, and a selection of element-intensity log-ratios. Note that all measured and predicted numerical variables are supplied with a 95% confidence interval. The precision of the log-ratios of intensities is so high that these are nearly invisible.

5.1. Lithofacies and poro-perm trends

The spatial distribution of predicted lithofacies differs slightly from the initial assignment. The main differences are associated with (previously unidentified) intercalations between different LAs and the occurrence of internal heterogeneities. Interfingering of lithofacies occurs for example between 3695.0 and 3693.5 m depth (LA-1 and LA-2), and

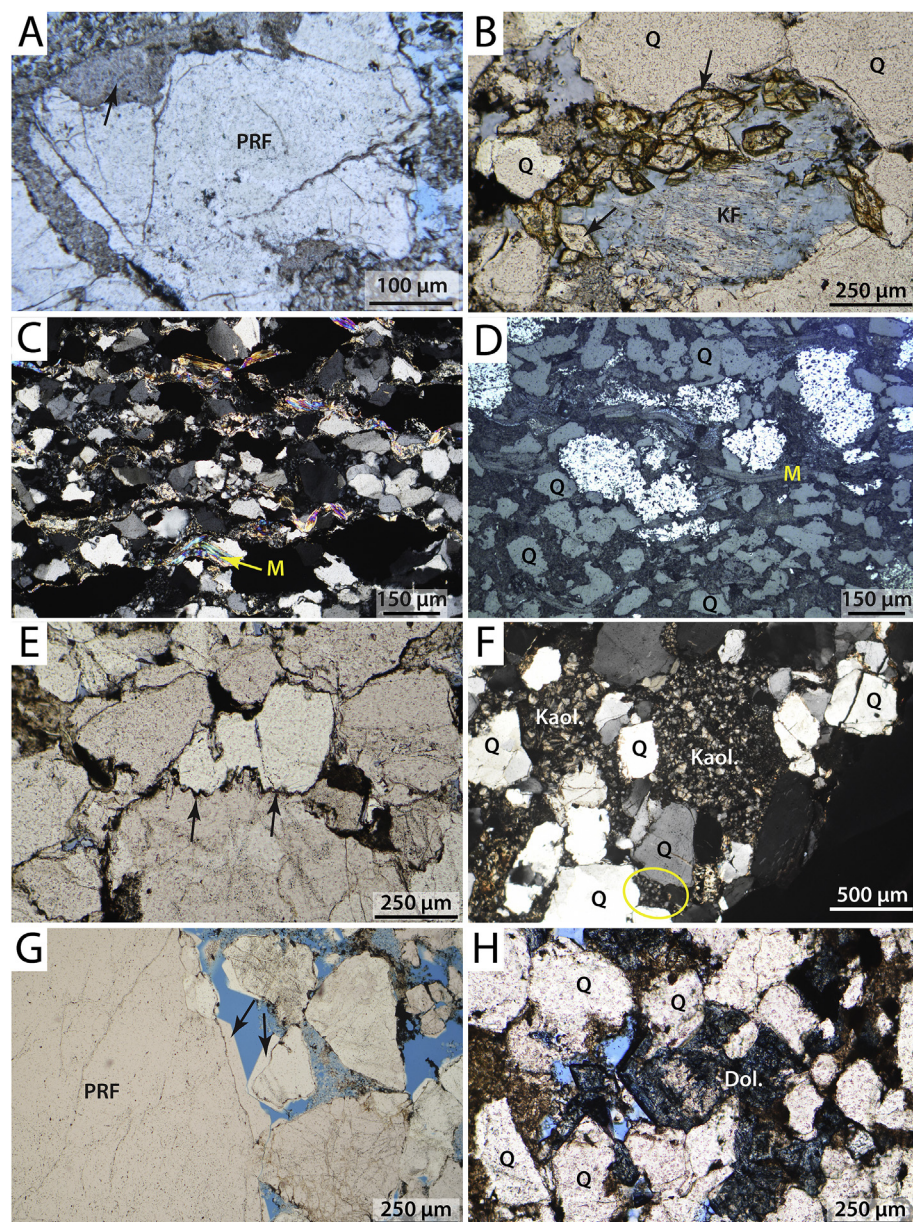


Fig. 5. Photomicrographs showing main detrital and diagenetic features. A) Plutonic rock fragment (PRF) in upper LA-2 composed of quartz and illitized K-feldspar crystals (arrow). Parallel nicols (sample 97; 3671.94 m depth). B) Relicts of a K-feldspar grain (KF) showing honeycomb secondary porosity and partial replacement by lozenge-shaped siderite (arrow). Upper LA-2. Q: detrital quartz grains. Parallel nicols (sample 97; 3671.94 m depth). C) Fine-grained interval in lower LA-3 with abundant mechanically deformed micas (arrow; M) and pyrite-replaced clay clasts. Crossed nicols (sample 144; 3683.75 m depth). D) Fine-grained interval in upper LA-3 showing frambooidal pyrite associated with clay clasts. Reflected light (sample 83, 3668.5 m depth). E) Pressure-solution sutured contact (i.e. stylolite) between quartz framework grains. Note the presence of dark clay particles at the contact (arrows). Lower LA-2. Parallel nicols (sample 180; 3692.75 m depth). F) Replacive (in oversized secondary pores) and pore-filling (solid circle) coarse-sized kaolinite (Kaol.) in upper LA-2. Crossed nicols (sample 124; 3678.73 m depth). G) Well-developed quartz overgrowths (arrows) in lower LA-2. Parallel nicols (sample 158; 3687.25 m depth). H) Zoned pore-filling Fe-dolomite cement in lower LA-3. Parallel nicols (sample 136; 3681.75 m depth).

between 3685.4 and 3684.0 m depth (LA-2 and LA-3). At 3682 m depth, there is a thin interval (orange coloured) within LA-3 which shows features typical of LA-1.

In the downcore poro-perm logs (Fig. 7), the match between the calibration samples (red dots) and the predicted poro-perm values is excellent. Predictions are unbiased and the prediction uncertainty (the grey band around the predicted values depicts the 95% confidence limits) is narrow. As expected, differences between the mean porosity and permeability values of the LAs before and after integration are not spectacular (Table 2). The predicted permeability values of LA-2 and LA-3 are slightly lower than the corresponding values of the raw data, and the same applies to the predicted porosity values of LA-3. Overall, the petrophysical definition of the three LAs has improved (Fig. 3D–F).

The vertical distribution patterns of both LA-2 intervals differ greatly (Fig. 7), despite their similar mean poro-perm values (Table 2, Fig. 3E). The lower LA-2 interval shows a more irregular trend than the blocky-shaped upper one. Both intervals of LA-3 are characterized by an upward-decreasing poro-perm trend, with the lower one displaying an irregular pattern in the bottom part.

5.2. Petrographically constrained geochemical analysis

In the log-ratios of element intensities of Fig. 7, Si has been used as common denominator because of its uniform pattern across the entire cored interval which accentuates variations in the numerator. Arbitrary cut-off lines were drawn in the log-ratio patterns to facilitate visual interpretation of the variation along core. The colour code represents the predominance of the numerator element relative to the denominator element (blue-coloured patterns) or vice versa (yellow-coloured patterns). The log-ratios of LA-1 show a high abundance of Ca relative to Si across the entire interval. The other log-ratios of LA-1 and all the log-ratios of the two LA-2 intervals show a predominance of Si over Al, K, Fe, Ca, Rb and Ti. Similar to the poro-perm patterns, the LA-2 interval of RU-1 shows more irregular log-ratio curves than the LA-2 interval of RU-2. In LA-3, elements such as Al, K, Fe, Ti, and to a minor extent, Ca and Rb tend to predominate over Si in most parts of the two RUs with a clear increasing-upwards trend in RU-2.

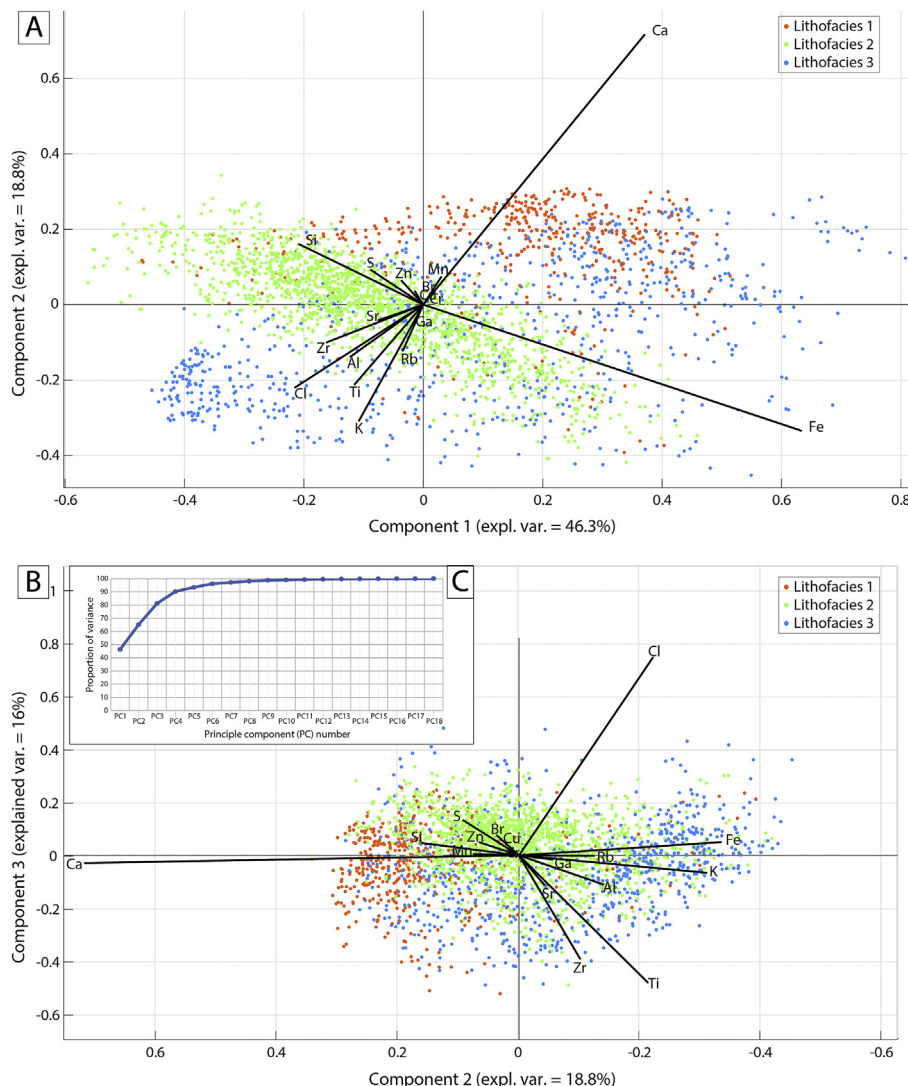


Fig. 6. Principal Component Analysis of the chemical intensities colour-coded according to original LA. A) Biplot showing PC1 versus PC2. B) Biplot showing PC2 versus PC3. C) Cumulative proportion of variance explained by the PCs. (For interpretation of the references to colour in this figure legend, the reader is referred to the Web version of this article.)

5.3. Correlation biplot

The effective integration of all properties allows us to provide a robust summary of the potential controls on RQ variation. Three statistically independent log-ratios of element intensities (which do not share any components) have been used to summarize the main patterns in the integrated data set. They were defined in accordance with their likely petrographic affinity as reported in the literature (Craigie, 2018 and references therein) and the qualitative thin-section analysis. Mean grain size is represented by $\ln\{\text{Si}/\text{Al}\}$, because Si is mainly associated with quartzose framework grains and Al is taken to represent the clay fraction; $\ln\{\text{Ca}/\text{Fe}\}$ reflects the abundance of late carbonate cements (Ca) relative to haematite/pyrite (Fe); and $\ln\{\text{Ti}/\text{Rb}\}$ is used as a proxy of the ratio between heavy minerals and clay. Colour codes of data points refer to predicted lithofacies class. The three log-ratios of element intensities have been combined with the predicted porosity and permeability values. All variables were standardized to produce a correlation biplot (Fig. 8).

The strong positive correlation among porosity, permeability and grain size ($\ln\{\text{Si}/\text{Al}\}$) is particularly evident in LA-2. This LA has the highest mean poro-perm values (14.5% and 6.7 mD, respectively; Table 2) and contains the coarsest sediments. In fact, its strong

association with Si (Fig. 6) and, consequently, its low $\ln\{\text{Al}/\text{Si}\}$ values in Fig. 7 (and its high $\ln\{\text{Si}/\text{Al}\}$ values in Fig. 8) point to the presence of quartz pebble stringers and dispersed granules, which are most abundant in the lower LA-2 interval.

The fairly low scores of LA-2 data points on $\ln\{\text{Ca}/\text{Fe}\}$ in Fig. 8 (equivalent to the high scores on Fe in Fig. 6) likely reflects the absence of carbonate cements ($\ln\{\text{Ca}/\text{Si}\}$ in Fig. 7) and the occurrence of clay rip-up clasts and pebbles which tend to be replaced by haematite and pyrite. The other main diagenetic products identified in LA-2 intervals consist of (locally) microporous replacive kaolinite and quartz overgrowths which may have contributed, to some extent, to the preservation of primary porosity (Fig. 5G). Quartz overgrowths are likely to have been locally sourced by chemical compaction.

A minor provenance change between RU-1 and RU-2 may be inferred from the increase in plutonic rock fragments in the upper LA-2, as suggested by petrographic examination. However, a petrophysical distinction between lower and upper LA-2 does not seem to offer any added value after data integration.

LA-1 is strongly associated with $\ln\{\text{Ca}/\text{Fe}\}$, likely due to the occurrence of carbonate cements as the most distinctive petrographic feature (Fig. 8). This is confirmed by the systematic association of LA-1 with Ca and Mn (Fig. 6) and the relative abundance of Ca over Si across

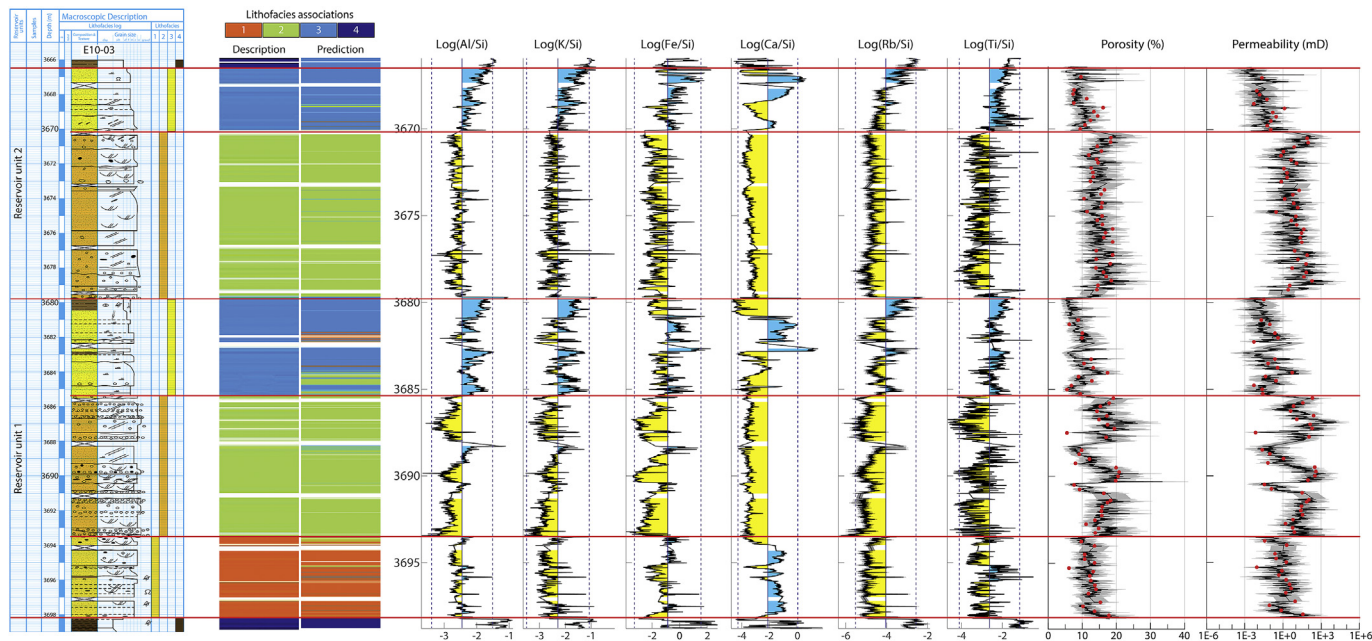


Fig. 7. Downcore variability of integrated datasets at 1-cm resolution. From left to right: sedimentary core description; original and predicted LAs; selected log-ratios of element intensities (Al/Si ; K/Si ; Fe/Si ; Ca/Si ; Rb/Si and Ti/Si); and predicted poro-perm logs with calibration samples marked as red dots. The grey bands around the measured values of log-ratio element intensities and predicted values of petrophysical quantities represent 95% confidence limits. Note that the high reproducibility of log-ratio element intensities implies that confidence limits are nearly invisible in most cases, except for $\log\{\text{Rb}/\text{Si}\}$. (For interpretation of the references to colour in this figure legend, the reader is referred to the Web version of this article.)

most part of the interval (Fig. 7). In this LA, carbonate cements mainly occur in secondary pores after K-feldspar dissolution or replacement (note the inverse correlation between Ca and K in Fig. 6), which probably has a minor impact on deterioration of porosity and permeability (Fig. 8). This assumption is also supported by the independent behaviour of the downcore $\ln\{\text{Ca}/\text{Si}\}$ and poro-perm patterns (Fig. 7).

LA-3 shows the lowest mean porosity and permeability values (8.5% and 0.03 mD, respectively; Table 2; Fig. 8). This poorer reservoir quality likely results from the combination of: (1) the overall finer grain size along the studied cored interval; (2) the occurrence of fining-upward trends and the associated upward increase of detrital mica and clay matrix contents; and (3) the presence of carbonate cements. The abundance of clay and the grain-size variation within this lithofacies

are corroborated by the inverse correlation with $\ln\{\text{Si}/\text{Al}\}$ (Fig. 8) and the strong association with the Al, K, Rb, Ga, Sr, Ti and Zr group in Fig. 6. The vertical distribution of clay-rich beds in the LA-3 interval of RU-1, depicted by $\ln\{\text{Al}/\text{Si}\}$, $\ln\{\text{K}/\text{Si}\}$ and $\ln\{\text{Rb}/\text{Si}\}$ patterns in Fig. 7, is consistent with the occurrence of several fining-upward trends. The LA-3 interval in RU-2 represents a single fining-upward trend.

5.4. Interfingering of lithofacies associations

The main difference between the operational definitions of LAs used for the macroscopic core description and the prediction of LAs is that the latter are geochemically constrained through their association with the XRF-CS record. Chemical variation within LAs reflects diagenetic

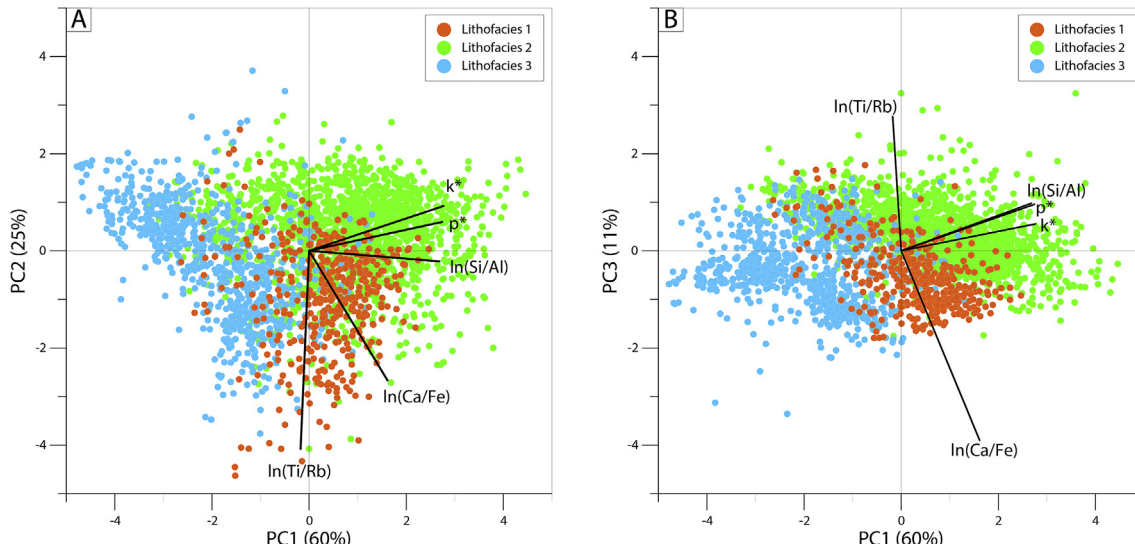


Fig. 8. Correlation biplot showing the predicted values of porosity (p^*) and permeability (k^*) and the most relevant chemical log-ratios, colour-coded according to predicted LA. (For interpretation of the references to colour in this figure legend, the reader is referred to the Web version of this article.)

heterogeneity as well as small-scale grain-size variability, both of which are strongly correlated with petrophysical properties (Fig. 7).

The minor occurrence of clay in LA-1 is indicated by discrete peaks of Al, K, Fe, Rb and Ti over Si (e.g. 3695.0 and 3693.5 m depth; Fig. 7). These clayey intervals correspond to single fine-grained layers and lags of Fe-oxidized rip-up clasts similar to those in LA-2. The result after data integration is a subtle interfingering between LA-1 and LA-2 (Figs. 7 and 8).

In LA-2, a 20-cm-thick interval can be observed around 3688.5 m depth in which Al and K are both high relative to Si. This interval has been identified as an alternation of LA-2 and LA-3 (interfingering) in the lithofacies prediction (Fig. 7).

In the LA-3 interval of RU-1, there is a marked enrichment of Ca relative to Si at 3682 m depth, which coincides with the thin bed that resembles LA-1 according to the lithofacies prediction. The overlap between LA-3 and LA-1 in Fig. 6 thus likely reflects the presence of carbonate cements, testifying to diagenetic heterogeneity within the lower LA-3. Between 3684 and 3685 m depth, lithofacies predictions show the presence of LA-2 intervals within LA-3. These are coarse-grained with low values of Ca, Rb, Ti over Si, and relatively high poro-perm values.

6. Discussion

6.1. Information content of high-resolution proxy record

An important requirement for successful prediction of sediment properties is that the high-resolution proxy record used to tie all RCA together should contain information which can be confidently related to the properties of interest. Appropriate transformation of the XRF-CS data renders them useful proxies of the chemical composition of siliciclastic sediments (Weltje and Tjallingii, 2008; Weltje et al., 2015). Chemical composition of siliciclastic sediments tends to vary with grain size on account of the fact that their mineral composition is strongly grain-size dependent (Weltje and von Eynatten, 2004). Hence, grain-size distributions can be predicted from geochemical data with an appropriate statistical model, as demonstrated by Bloemsma et al. (2012). The correlation between grain-size distribution and petrophysical properties such as porosity and permeability has also been established, both experimentally (e.g. Beard and Weyl, 1973) and theoretically (Panda and Lake, 1994), which implies these quantities can also be predicted from chemical (proxy) data of siliciclastic sediments. In view of the inter-relations among properties, it is conceivable that other types of high-resolution (hyper)spectral data such as Near Infrared Reflectance spectroscopy (NIR), which are sensitive to mineralogical composition (Hahn et al., 2018) may possess comparable predictive power.

6.2. Added value of ICA

The common approach to upscaling of RCA data is to statistically characterise the petrophysical properties of each lithofacies by the mean and variance of porosity and permeability (McPhee et al., 2015; Tavakoli, 2018), analogous to Table 2 and Fig. 3. In this conventional approach, the continuous sedimentological log cannot be quantitatively exploited to shed more light on the spatial (vertical) variability of petrophysical properties within and between each lithofacies class, and the potential geological heterogeneity of the reservoir units targeted by the well cannot be assessed. For this, a straightforward example is selected of a reservoir interval that would have been easily identified on wireline logs, and subdivided into several units. The added value of ICA is that it brings out small-scale heterogeneities within such units that cannot be detected with conventional wireline logs that have decimeter-scale resolution.

In the ICA approach, predictions are generated in a multivariate space defined by the properties measured at each sampling location

(element intensities, porosity, permeability, and assigned lithofacies), which implies that no spatial information (i.e. core depth) is used. The high-resolution spatial variability of properties obtained by placing the data points in the right order along a core thus provides additional information on the spatial continuity of the predictions, which may be used to assess their feasibility. Prediction of petrophysical properties at high spatial resolution permits the internal heterogeneity of LAs to be evaluated, which provides deeper insights into the geological controls on the spatial distribution of reservoir quality within units.

The three main controls on reservoir quality, as summarized in Fig. 8, may be equated to the first three principal components responsible for 96% of the joint petrographic and petrophysical variability: (1) the grain size distribution, (2) the presence of clay, both detrital (as clay pebbles or silty clay layers) and diagenetic (as kaolinite and illite), and (3) the abundance of carbonate cements. Inspection of these patterns along the core permits a refinement of the reservoir zonation model by identifying grain size trends, interfingering of LAs, and the presence of carbonate-cemented layers.

Depositional and diagenetic heterogeneities have a key significance in the interpretation of depositional setting if they can be shown to support the sedimentological model. An example of this is the presence of a carbonate-rich LA-1 prone interval recognized within LA-3 of RU-1 after the data integration. Thin calcretes and paleosols are often formed on top of abandoned crevasse splay lobes during subaerial exposure (Van Toorenburg et al., 2016).

Despite the fact that logratios of element intensities are highly reproducible, some authors (e.g. Craigie, 2018) dismiss XRF-CS for geochemical logging based on the (perceived) analytical superiority of conventional destructive chemical analysis. Such assessments do not take into account that the sheer size of XRF-CS data sets greatly facilitates the appropriate application of robust exploratory statistical methods (Kelloway et al., 2014), as indicated in the example where the petrophysical signatures of the three LAs could be better delineated on the basis of predicted properties than from the original plug data. The reason for this is that the RCA data set is of limited size and has not been integrated with the sedimentological core description.

6.3. Sampling errors

The MSPE based on cross-validation is used to establish 95% confidence regions around the predictions in the poro-perm logs (grey band; Fig. 7). The width of this region reflects the quality of the prediction which may be influenced by three sources of sampling error:

1. Sample size and representativeness: the quality of calibration increases with the number of samples, provided they have been selected according their intensity spectra in the clr-space to cover the range of chemical variation in the data (Weltje et al., 2015). For the sake of robustness, other factors of interest must be contemplated to ensure the representativeness of the calibration data, such as the range of petrophysical properties, lithofacies and grain sizes considered.
2. Positioning errors: with increasing resolution, inaccuracies of positioning (depth coordinates) of the data sets to be integrated tend to become an issue, especially in the case of legacy data. The resolution adopted in this study (1 cm) coincides with the RCA plug diameter from which standard core studies derive the petrophysical data (McPhee et al., 2015), and represents a natural trade-off between reduction of positioning errors and highest desirable resolution.
3. Irreducible sampling errors: the volumes corresponding to XRF measurements, core plugs, and thin sections are non-overlapping. The magnitude of irreducibility is ruled by the grain size of the sediments, because the representativeness of the average chemical composition measured at a certain position is inversely proportional to a sediment's bedding-parallel heterogeneity (i.e. the coarser the sediment, the higher the risk of measuring a single mineral grain/

phase).

The prediction generated by the ICA workflow takes into account the abovementioned potential sources of error by making use of cross validation. Therefore, predictions are always statistically correct (i.e. approximately 95% of the data points are expected to be contained with the 95% confidence region) but not necessarily highly precise, if the data set used for calibration is small and/or not fully representative.

7. Conclusions

The objective of Integrated Core Analysis (ICA) is to improve reservoir quality prediction through optimization of the routine core analysis (RCA) workflow. This is achieved by fusing RCA data with high-resolution XRF core scans to generate near-continuous multivariate time series of sediment properties with quantified uncertainties. This “downscaling” operation permits maximization of the combined geological-petrophysical information that can be extracted from cores.

The Integrated Core Analysis (ICA) methodology is based on an internally consistent statistical framework that enables advanced multivariate calibration and property-prediction algorithms to be used with maximum effect. It also permits prediction errors to be quantified, and thus objectively evaluate the value of predicted core data.

Petrographic analysis of the initial grain assemblage and its diagenetic modifications is indispensable for guiding interpretation of the near-continuous XRF-CS record based on element-mineral affinities.

The operational definition of lithofacies associations (which includes the criterion of “mappability” along core at a given resolution) is crucial to reservoir-quality prediction and relies on correct identification of depositional mechanisms and environments. The ICA protocol permits testing of operational definitions by downscaling the core description to the resolution of the XRF-CS data.

ICA of the studied Upper Carboniferous (early Westphalian B) fluvial reservoir sandstones reveals distinct compositional and petrophysical trends within each lithofacies association and marked changes at lithofacies boundaries. The ICA workflow thus greatly facilitates definition of sedimentologically and petrophysically valid “mappable” reservoir zones.

The ICA methodology is highly suitable for re-assessing legacy data comprising multiple cores from a single reservoir unit, which have been acquired over a span of time in which data-acquisition conventions have evolved. Such heterogeneous data sets can be harmonized to a single (XRF-CS) standard to provide an internally consistent description of their main sedimentological and petrophysical signatures.

Authorship

S. Henares contributed to the design of the study, data acquisition and processing, and writing of the manuscript. M.E. Donselaar contributed to data acquisition and processing, and writing. M.R. Bloemsma contributed to conceptualisation of the method, data processing, and critical revision of the manuscript. R. Tjallingii contributed to data acquisition and critical revision. B. De Wijn critically revised the manuscript. G.J. Weltje contributed to conceptualisation of the method, data processing, and writing.

Acknowledgements

The authors gratefully acknowledge Wintershall Noordzee BV, Nederlandse Aardolie Maatschappij BV, Shell BV, and Energie Beheer Nederland for financially supporting this study. Core material was kindly provided by Wintershall Noordzee BV. The Associated Editor S. Critelli and R. Worden are also thanked for the useful comments that contributed to improve the manuscript.

Appendix A. Supplementary data

Supplementary data to this article can be found online at <https://doi.org/10.1016/j.marpetgeo.2019.07.034>.

References

- Abdi, H., 2010. Partial least squares regression and projection on latent structure regression (PLS Regression). *WIREs Comput. Stat.* 2, 97–106.
- Aitchison, J., 1986. *The Statistical Analysis of Compositional Data*. Monographs on Statistics and Applied Probability. Chapman & Hall Ltd., London, pp. 416 reprinted in 2003 by the Blackburn Press, New Jersey (1986).
- Bakker, E., Pruno, S., 2004. Conventional and Special Core Analysis on Cores from Well E10-3XX. Panterra Geoconsultants. Report No. c0222, 20 p. Netherlands Oil and Gas portal. <http://www.nlog.nl/en>.
- Baraka-Lokmane, S., Main, I.G., Ngwenya, B.T., Elphick, S.C., 2009. Application of complementary methods for more robust characterization of sandstone cores. *Mar. Pet. Geol.* 26, 39–56.
- Beard, D.C., Weyl, P.K., 1973. Influence of texture on porosity and permeability of unconsolidated sand. *AAPG (Am. Assoc. Pet. Geol.) Bull.* 57, 349–369.
- Bloemsma, M.R., 2015. Development of a Modelling Framework for Core Data Integration Using XRF Scanning. PhD dissertation. Delft University of Technology, Delft, pp. 217. Xelerate software package: www.mennobloemsma.nl/software.php.
- Bloemsma, M.R., Zabel, M., Stuit, J.B.W., Tjallingii, R., Collins, J.A., Weltje, G.J., 2012. Modelling the joint variability of grain-size and chemical composition in sediments. *Sediment. Geol.* 280, 135–148 (+ Erratum: 284–285, 214).
- Bloemsma, M.R., Croudace, I., Daly, J.S., Edwards, R.J., Francus, P., Galloway, J.M., Gregory, B.R.B., Huang, J.-J.S., Jones, A.F., Kylander, M., Löwemark, L., Luo, Y., MacLachlan, S., Ohlendorf, C., Patterson, R.T., Pearce, C., Profe, J., Reinhardt, E.G., Stranne, C., Tjallingii, R., Turner, J.N., 2018. Practical guidelines and recent advances in the Itrax XRF core-scanning procedure. *Quat. Int.* <https://doi.org/10.1016/j.quaint.2018.10.044>.
- Boels, J., 2003. Sedimentology, Petrography and Reservoir Quality of the Upper Carboniferous in well E10-3. Panterra Geoconsultants. Report No. G453, 98 p. Netherlands Oil and Gas portal. <http://www.nlog.nl/en>.
- Craigie, N., 2018. Principles of elemental chemostratigraphy: a practical user guide. In: Swennen, R. (Ed.), *Advances in Oil and Gas Exploration & Production*. Springer-Verlag, Berlin, pp. 196.
- Croudace, I.W., Rindby, A., Rothwell, R.G., 2006. ITRAX: description and evaluation of a new multi-function X-ray core scanner. In: Rothwell, R.G. (Ed.), *New Techniques in Sediment Core Analysis*. vol. 267. Geological Society of London Special Publications, pp. 51–63.
- De Jong, S., 1993. SIMPLS: an alternative approach to partial least squares regression. *Chemometr. Intell. Lab. Syst.* 18, 251–263.
- Fielding, C.R., Alexander, J., Allen, J.P., 2018. The role of discharge variability in the formation and preservation of alluvial sediment bodies. *Sediment. Geol.* 365, 1–20.
- Geluk, M.C., de Haan, H., Nio, S.D., Schroot, B., Wolters, B., 2002. The permo-carboniferous gas play, southern North Sea, The Netherlands. In: In: Hills, L.V., Henderson, C.M., Bamber, E.W. (Eds.), *Proceedings XIV International Congress on the Carboniferous and Permian*, August 17–21, 1999, Calgary, Canada, vol. 19. Canadian Society of Petroleum Geologists Memoir, pp. 877–894 Carboniferous and Permian of the world.
- Griffiths, J.C., 1961. Measurement of the properties of sediments. *J. Geol.* 69, 487–498.
- Hahn, A., Vogel, H., Andó, S., Garzanti, E., Kuhn, G., Lantzsch, H., Schüürman, J., Vogt, C., Zabel, M., 2018. Using Fourier transform infrared spectroscopy to determine mineral phases in sediments. *Sediment. Geol.* 375, 27–35.
- Henares, S., Weltje, G.J., Donselaar, M.E., Bloemsma, M.R., Tjallingii, R., de Wijn, B., 2018. From routine to integrated core analysis: setting up the database for reservoir quality modelling. In: 80th EAGE Conference and Exhibition, Copenhagen, Denmark, 11–14 June, <https://doi.org/10.3997/2214-4609.201801136>.
- Jansen, J.H.F., Van der Gaast, S.J., Koster, B., Vaars, A.J., 1998. CORTEX, a shipboard XRF scanner for element analyses in split sediment cores. *Quat. Res.* 151, 143–153.
- Kelloway, S., Ward, C.R., Marjo, C.E., Wainwright, I.E., Cohen, D.R., 2014. Quantitative chemical profiling of coal using core-scanning X-ray fluorescence techniques. *Int. J. Coal Geol.* 128–129, 55–67.
- Kosters, M., Donselaar, M.E., 2003. Syn-sedimentary faulting and the formation of localized reservoir sands: Carboniferous examples from the Campine Basin, Belgium and the Dutch offshore. *Pet. Geosci.* 9, 309–319.
- Lachenbruch, P.A., Goldstein, M., 1979. Discriminant analysis. *Biometrics* 35, 69–85.
- McPhee, C., Reed, J., Zubizarreta, I., 2015. *Core Analysis: a Best Practice Guide. Developments in Petroleum Science*, vol. 64. Elsevier, United Kingdom, pp. 852.
- Panda, M.N., Lake, L., 1994. Estimation of single-phase permeability from parameters of particle-size distribution. *AAPG (Am. Assoc. Pet. Geol.) Bull.* 78, 1028–1039.
- Reijers, T.J.A., Mijnlieff, H.F., Pestman, P.J., Kouwe, W.F.P., 1993. Lithofacies and their interpretation: a guide to standardised description of sedimentary deposits. *Meded. Rijks Geol. Dienst* 49, 55.
- Richter, T.O., Van der Gaast, S., Koster, B., Vaars, A., Gieles, R., de Stigter, H.C., de Hass, H., van Weering, T.C.E., 2006. The Avaatech XRF core scanner: technical description and applications to NE Atlantic sediments. In: In: Rothwell, R.G. (Ed.), *New Techniques in Sediment Core Analysis*, vol. 267. Geological Society of London Special Publications, pp. 39–50.
- Tavakoli, V., 2018. *Geological Core Analysis. Application to Reservoir Characterization*. Springer-Verlag, pp. 106.
- Tjallingii, R., Röhli, U., Kölling, M., Bickert, T., 2007. Influence of the water content on X-

- ray fluorescence core-scanning measurements in soft marine sediments. *Geochem. Geophys. Geosyst.* 8 (2). <https://doi.org/10.1029/2006GC001393>.
- Van Adrichem Boogaert, H., Kouwe, W., 1993. Stratigraphic nomenclature of The Netherlands, revision and update by Rijks geologische dienst (RGD) and Netherlands oil and gas exploration and production association (NOGEPA). *Meded. Rijks Geol. Dienst* 50, 1–180.
- Van Toorenburg, K.A., Donselaar, M.E., Noordijk, N.A., Weltje, G.J., 2016. On the origin of crevasse-splay amalgamation in the Huesca fluvial fan (Ebro Basin, Spain): implications for connectivity in low net-to-gross fluvial deposits. *Sediment. Geol.* 343, 156–164.
- Van Toorenburg, K.A., Donselaar, M.E., Weltje, G.J., 2018. The life cycle of crevasse splays as a key mechanism in aggrading dryland rivers. *Earth Surf. Process. Landforms* 43, 2409–2420.
- Weltje, G.J., Bloemsma, M., Henares, S., Donselaar, M.E., 2017. Integrated Core Analysis: Automated Mapping of Diagenetic Anomalies and Provenance Changes for Reservoir Quality Assessment. 33rd IAS, Toulouse, France, 10–12 October. Abstract Book, pp. 966.
- Weltje, G.J., Bloemsma, M.R., Tjallingii, R., Heslop, D., Röhl, U., Croudace, I.W., 2015. Prediction of geochemical composition from XRF core scanner data: a new multi-variate approach including automatic selection of calibration samples and quantification of uncertainties. In: Croudace, I.W., Rothwell, R.G. (Eds.), *Micro-Xrf Studies of Sediment Cores, Developments in Palaeoenvironmental Research*. Springer, Berlin Heidelberg, pp. 507–534.
- Weltje, G.J., Tjallingii, R., 2008. Calibration of XRF core scanners for quantitative geochemical logging of sediment cores: theory and application. *Earth Planet. Sci. Lett.* 274, 423–438.
- Weltje, G.J., von Eynatten, H., 2004. Quantitative provenance analysis of sediments: review and outlook. *Sediment. Geol.* 171, 1–11.
- Ziegler, P.A., 1990. *Geological Atlas of Western and Central Europe*, second ed. Geological Society of London, Publication House, Bath, pp. 239 56 encls.